Prevalent mechanism of membrane bridging by synaptotagmin-1

Alpay B. Seven[a], Kyle D. Brewer[a], Liang Shi[b], Qiu-Xing Jiang[b], and Josep Rizo[a,1]

[a]Departments of Biophysics, Biochemistry, and Pharmacology and [b]Department of Cell Biology, University of Texas Southwestern Medical Center, Dallas, TX 75390

Edited* by Thomas C. Südhof, Stanford University School of Medicine, Stanford, CA, and approved July 10, 2013 (received for review May 30, 2013)

Synaptotagmin-1 functions as a Ca^{2+} sensor in neurotransmitter release through its two C_2 domains (the C_2A and C_2B domain). The ability of synaptotagmin-1 to bridge two membranes is likely crucial for its function, enabling cooperation with the soluble N-ethylmaleimide sensitive factor adaptor protein receptors (SNAREs) in membrane fusion, but two bridging mechanisms have been proposed. A highly soluble synaptotagmin-1 fragment containing both domains (C_2AB) was shown to bind simultaneously to two membranes via the Ca^{2+}-binding loops at the top of both domains and basic residues at the bottom of the C_2B domain (direct bridging mechanism). In contrast, a longer fragment including a linker sequence (lnC_2AB) was found to aggregate in solution and was proposed to bridge membranes through *trans* interactions between lnC_2AB oligomers bound to each membrane via the Ca^{2+}-binding loops, with no contact of the bottom of the C_2B domain with the membranes. We now show that lnC_2AB containing impurities indeed aggregates in solution, but properly purified lnC_2AB is highly soluble. Moreover, cryo-EM images reveal that a majority of lnC_2AB molecules bridge membranes directly. Fluorescence spectroscopy indicates that the bottom of the C_2B domain contacts the membrane in a sizeable population of molecules of both membrane-bound C_2AB and membrane-bound lnC_2AB. NMR data on nanodiscs show that a fraction of C_2AB molecules bind to membranes with antiparallel orientations of the C_2 domains. Together with previous studies, these results show that direct bridging constitutes the prevalent mechanism of membrane bridging by both C_2AB and lnC_2AB, suggesting that this mechanism underlies the function of synaptotagmin-1 in neurotransmitter release.

membrane bending | Ca2+ sensing | exocytosis | synaptic transmission

Neurotransmitter release is a key event in interneuronal communication that is acutely triggered by Ca^{2+} influx into a presynaptic terminal (1). The synaptic vesicle protein synaptotagmin-1 acts as a Ca^{2+} sensor in fast release through the two C_2 domains that form most of its cytoplasmic region (the C_2A and C_2B domains) (2–5). This function is coupled to membrane fusion through the neuronal soluble N-ethylmaleimide sensitive factor adaptor protein receptor (SNARE) proteins (6, 7), which bring the synaptic vesicle and plasma membranes together by forming SNARE complexes (2, 3). Synaptotagmin-1 function also depends on a tight interplay with complexins (8–10) and other key proteins of the release machinery (11, 12). The synaptotagmin-1 C_2 domains bind three or two Ca^{2+} ions through loops at the top of β-sandwich structures (13–15) (Fig. 1*A*). These top loops also mediate Ca^{2+}-dependent phospholipid binding (15–17), which is crucial for synaptotagmin-1 function (5, 18). Moreover, the synaptotagmin-1 cytoplasmic region clusters chromaffin granules and liposomes (19), and a fragment containing its two C_2 domains was shown by cryo-EM to bind simultaneously to two membranes, bringing them into close proximity (~4 nm) (20). The C_2B domain is sufficient for this activity (20), which can explain the preponderant role of Ca^{2+} binding to the C_2B domain in neurotransmitter release (21, 22). Mutation of two arginine residues at the bottom of the C_2B domain (R398 and R399) strongly impairs neurotransmitter release, the liposome-clustering activity, and the ability to stimulate SNARE-dependent lipid mixing between liposomes (7). These findings led to the proposal that synaptotagmin-1 cooperates with the SNAREs in inducing membrane fusion by helping to bring the two membranes together in a Ca^{2+}-dependent manner, directly bridging the two membranes via the Ca^{2+}-binding loops at the top and the arginines at the bottom of the C_2B domain (7, 20, 23).

Though EPR data agreed with this model of membrane bridging (24), and increasing evidence supports the notion that the membrane-bridging activity of synaptotagmin-1 is critical for its function (7, 25–31), a recent study concluded that the bridging occurs by a fundamentally different mechanism that requires *trans* interactions between synaptotagmin-1 oligomers bound to each membrane, without binding of the bottom of the C_2B domain to the lipids (29). This mechanism, which we refer to as the oligomerization model, is compared in Fig. 1 *B* and *C* with the direct-bridging model. The oligomerization model was supported in part by 7-nitrobenz-2-oxa-1,3-diazole (NBD) fluorescence data that contradicted our previous NBD fluorescence results (20) and suggested that the bottom of the C_2B domain does not contact the membranes (29). Cryo-EM images reported in a separate study (25) revealed a separation of ~9 nm between synaptotagmin-1 bridged membranes, consistent with the oligomerization model. Note, however, that both of these studies used a synaptotagmin-1 fragment containing the two C_2 domains and most of the linker that separates them from the vesicle membrane (residues 95–421 and 96–421 in refs. 25 and 29, respectively; below we refer to both as lnC_2AB), whereas the fragment that we used contained only the two C_2 domains (residues 140–421; below referred to as C_2AB) (20).

Significance

The ability of synaptotagmin-1 to bridge two membranes is likely critical for its function as a Ca^{2+} sensor in neurotransmitter release. A synaptotagmin-1 fragment spanning its two C_2 domains bridges membranes directly, binding simultaneously to both membranes. However, a longer synaptotagmin-1 fragment spanning most of its cytoplasmic region was proposed to bridge membranes through protein–protein interactions between oligomers bound to each membrane. This paper now shows that direct bridging actually constitutes the prevalent mechanism of membrane bridging by the longer synaptotagmin-1 fragment. These findings strongly suggest that direct membrane bridging underlies the function of synaptotagmin-1 in neurotransmitter release.

Author contributions: A.B.S., K.D.B., Q.-X.J., and J.R. designed research; A.B.S., K.D.B., L.S., and J.R. performed research; A.B.S., K.D.B., Q.-X.J., and J.R. analyzed data; and A.B.S., K.D.B., Q.-X.J., and J.R. wrote the paper.

The authors declare no conflict of interest.

*This Direct Submission article had a prearranged editor.

[1]To whom correspondence should be addressed. E-mail: jose@arnie.swmed.edu.

This article contains supporting information online at www.pnas.org/lookup/suppl/doi:10.1073/pnas.1310327110/-/DCSupplemental.

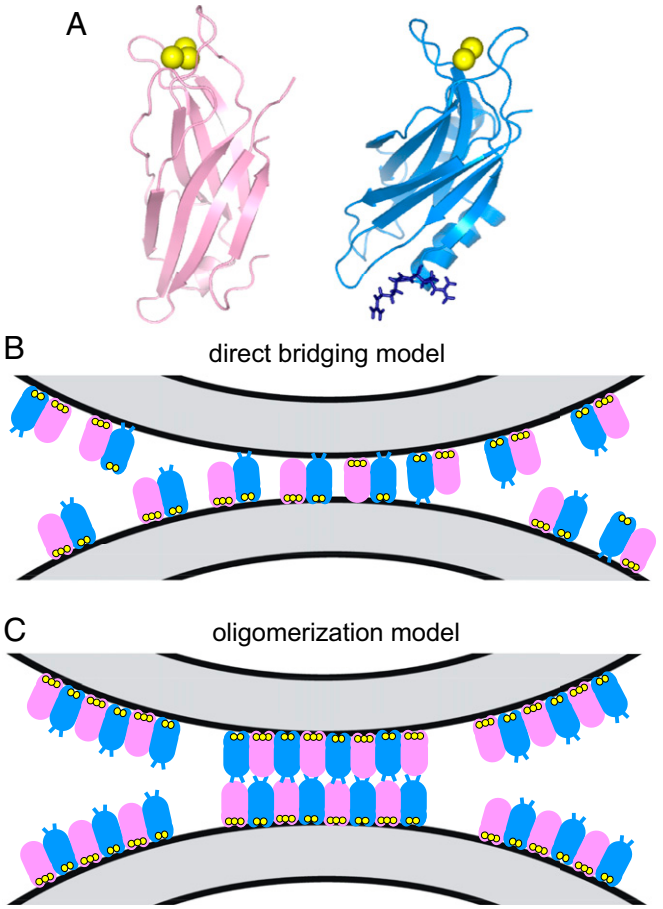

Fig. 1. Two models of membrane bridging by synaptotagmin-1. (*A*) Ribbon diagrams of the synaptotagmin-1 C_2A domain (40) (*Left*) and C_2B domain (15) (*Right*). Ca^{2+} ions are shown as yellow spheres. The two arginines at the bottom of the C_2B domain (R398 and 399) are shown as blue stick models. (*B*) Direct-bridging model whereby the C_2 domains bind simultaneously to the two apposed membranes, resulting in an intermembrane distance of ~4 nm. The C_2A and C_2B domains are shown in pink and blue, respectively, with the Ca^{2+} ions bound to the top loops in yellow; the R398 and R399 side chains at the bottom of the C_2B domain are represented by blue lines. The diagram is meant to illustrate that the two C_2 domains can have parallel or antiparallel orientations, with the Ca^{2+}-binding loops binding to the same membrane or to opposite membranes; R398 and R399 can cooperate in bridging in both orientations, but are more critical for bridging in the parallel orientation. Bridging requires multiple C_2AB molecules but does not involve interactions between them (20). (*C*) Oligomerization model whereby bridging is mediated by *trans* interactions between oligomers bound to separate membranes, resulting in an intermembrane distance of ~8–9 nm. The model postulates that only the Ca^{2+}-binding loops contact the membranes, whereas R398 and R399 do not, instead mediating protein–protein interactions (29). The putative binding mode between oligomers is unknown, and hence the model of interactions between the bottom sides of the C_2 domains shown is arbitrary.

Clarifying these apparently conflicting results and defining how synaptotagmin-1 bridges membranes is crucial to understanding its mechanism of action in neurotransmitter release. With this double goal, we have investigated whether there are two mechanisms of membrane bridging and whether the C_2AB and lnC_2AB fragments have some different properties that might favor distinct mechanisms, focusing on particular aspects where results from different studies appeared to be contradictory. Together with previously available data, our results show that the direct model underlies the major mechanism of membrane bridging by both C_2AB and lnC_2AB. Moreover, NBD fluorescence spectroscopy and NMR analyses on nanodiscs show that a fraction of C_2AB molecules bind to membranes with antiparallel orientations of the C_2 domains and contact of the bottom of the C_2B domain with the membranes.

Results

Solubility of Synaptotagmin-1 Fragments. A potential reason for distinct behavior in synaptotagmin-1 fragments is a different solubility. Indeed, the study that proposed the oligomerization model (29) reported aggregation of lnC_2AB in solution at concentrations above 10 μM in the presence of 1 mM Ca^{2+}, a property that might underlie the putative oligomerization on membranes. This aggregation data contrasts with the high solubility of the C_2AB fragment that we have observed in extensive studies performed over the years under varied conditions, even at high protein and Ca^{2+} concentrations. This high solubility is illustrated, for instance, by the high quality of the ^{1}H-^{15}N transverse relaxation-optimized spectroscopy (TROSY)-heteronuclear single quantum coherence (HSQC) spectra that we obtain regularly for ^{15}N- or ^{2}H,^{15}N-labeled C_2AB (20, 23), or by the line widths observed in the ^{1}H NMR spectrum of 800 μM ^{15}N-labeled C_2AB shown in Fig. S1, which was obtained in 100 mM Ca^{2+}.

To investigate the behavior of lnC_2AB in our hands, we prepared ^{15}N-labeled lnC_2AB fragment using the same rigorous purification procedure that we commonly use for C_2AB and that includes affinity chromatography with washes at high salt and high Ca^{2+} concentrations, a benzonase treatment on the affinity column, ion exchange chromatography, and gel filtration (*Materials and Methods*). The ^{1}H-^{15}N TROSY-HSQC spectrum of purified 100-μM lnC_2AB in 20 mM Ca^{2+} (Fig. 2) exhibited similar quality to those obtained for C_2AB (20, 23), with an increased number of cross-peaks in the middle of the spectrum that can be attributed to the additional residues from the linker region and that indicate that this region is unstructured. Note that ^{1}H-^{15}N TROSY-HSQC spectra are very sensitive to aggregation and hence the high quality of the spectrum obtained for lnC_2AB shows that it has no detectable tendency to aggregate even in 20-mM Ca^{2+} and 100-μM protein concentration. This result is in stark contrast with the reported tendency of lnC_2AB to aggregate (29). However, we did notice that partially purified samples of lnC_2AB had a much higher tendency to aggregate in the presence of Ca^{2+} than the fully purified protein.

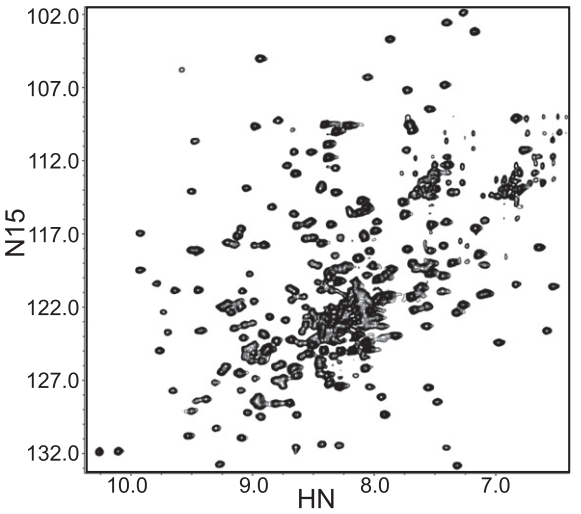

Fig. 2. Ca^{2+}-bound lnC_2AB yields high-quality NMR data. The contour plot shows a ^{1}H-^{15}N TROSY-HSQC spectra of 100 μM ^{15}N-lnC_2AB in 25 mM Tris (pH 7.4) containing 125 mM NaCl and 20 mM Ca^{2+}.

To analyze in more detail how purity may affect aggregation, we used the same turbidity assay that was used previously to monitor the aggregation tendency of lnC_2AB in solution (29). For this purpose, we prepared an lnC_2AB sample using our purification protocol, including the benzonase treatment, but we performed the final gel filtration step without the preceding ion exchange chromatography. We observed two major peaks, one that eluted at the volume corresponding to monomeric, pure lnC_2AB (peak 2; Fig. 3*A*) and another that eluted earlier (peak 1; Fig. 3*A*). Both peaks contained lnC_2AB (Fig. 3*A*, *Inset*), and reinjection into an analytical column showed that both peaks correspond to stable species (Fig. S2). The turbidity of the samples from both peaks as assessed from the absorbance at 400 nm was within background levels for both peak 1 and peak 2 in the absence of Ca^{2+}. For peak 2, the turbidity also remained at background levels in 1 mM Ca^{2+} even at 100-μM protein concentration (Fig. 3*B*, red triangles), as we observed also for an lnC_2AB sample purified by our complete protocol (Fig. 3*B*, black circles). Strikingly, the lnC_2AB sample corresponding to peak 1 exhibited a steep increase in turbidity in 1 mM Ca^{2+} at protein concentrations above 10 μM (Fig. 3*B*, blue squares), and the concentration dependence of turbidity was similar to that reported previously for lnC_2AB in the study that proposed the oligomerization model (29). Hence, we were not able to reproduce the reported aggregation of lnC_2AB using our fully purified lnC_2AB, but we did observe this aggregation behavior with partially purified lnC_2AB.

Whereas the UV spectrum of peak 2 exhibited a maximum at ∼280 nm, as is common for proteins, the maximum absorption in the UV spectrum of peak 1 was at ∼265 nm (Fig. 3*C*). This feature is typical of samples contaminated with nucleic acids and is common in partially purified synaptotagmin-1 fragments containing the C_2B domain because of its very high affinity for polyacidic compounds (32). Though elimination of such contaminants is particularly difficult for the isolated C_2B domain (15, 32), the C_2AB and lnC_2AB fragments also require special precautions for purification, as outlined above and described in more detail in *Materials and Methods*. In fact, most of the lnC_2AB protein elutes in early peaks in gel filtration if we do not perform the benzonase treatment, despite the fact that we perform washing steps with high salt on the affinity resin. In this context, it is important to note that the study that proposed the oligomerization model claimed to have removed polyacidic contaminants by high-salt washes on an affinity column (29). In our hands, this procedure is far from sufficient to obtain pure lnC_2AB. We also emphasize that in some occasions, ^{1}H-^{15}N HSQC spectra have revealed the presence of contaminants in the synaptotagmin-1 C_2B domain even when there was no unusual absorption maximum near 260 nm (33), showing that a lack of such an absorption maximum is not sufficient to ensure purity. Thus, we normally verify the purity of synaptotagmin-1 fragments including the C_2B domain using ^{1}H-^{15}N HSQC or TROSY-SQC spectra on ^{15}N-labeled samples (Fig. 2). Based on the signal-to-noise ratio of these spectra, we estimate that our procedure yields protein that is at least 95% free of contaminants.

Prevalence of Direct Membrane Bridging by lnC_2AB. The most direct evidence supporting the oligomerization model of membrane bridging by lnC_2AB was provided by cryo-EM images showing extended flat surfaces of liposomes apposed to each other with a constant separation of ∼9 nm, and clear electron density between them that can be attributed to lnC_2AB oligomers or aggregates (25). These images contrast with those that we obtained by cryoelectron tomography with C_2AB, where the predominant separation between apposed membranes was ∼4 nm, as expected for direct membrane bridging by a C_2 domain (20). We did observe some longer distances for some interfaces bridged by C_2AB, but they did not involve extended parallel surfaces and clear accumulation of oligomeric protein density between them. Note also that such longer distances are expected to arise naturally as liposomes approach before association or separate after dissociation given the dynamic nature of the liposome clustering induced by C_2AB (20).

To investigate the mechanism of membrane bridging by lnC_2AB in our own hands, we performed cryo-EM experiments with lnC_2AB and liposomes containing the same lipid composition used in ref. 25 (Fig. 4 and Fig. S3). Samples were prepared with a 1:120 lnC_2AB-to-lipid ratio, which is sufficient to induce liposome clustering (20, 29), or with an excess of lnC_2AB to yield an lnC_2AB-to-lipid ratio of 1:36, which further favors clustering. In none of the samples we observed the extended flat surfaces of liposomes apposed to each other that were reported in ref. 25, but note that it is unclear how prevalent this type of interface was in that study because no quantitative analysis of the cryo-EM

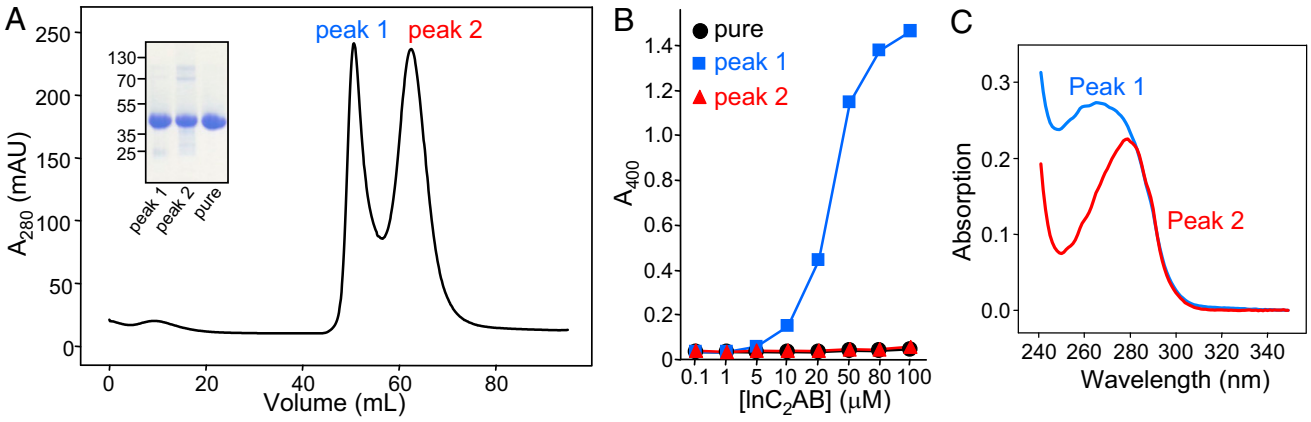

Fig. 3. Impurities promote aggregation of lnC_2AB in solution. (*A*) Gel filtration profile on a Superdex 75 16/60 column of an lnC_2AB sample that was purified by our usual procedure, including the benzonase treatment, but without ion exchange chromatography step. (*Inset*) Peaks 1 and 2, as well as a control sample of fully purified lnC_2AB (pure), were analyzed by SDS/PAGE and Coomassie blue staining. (*B*) Analysis of lnC_2AB aggregation using a turbidity assay. The turbidity as monitored from the absorption at 400 nm was measured as a function of protein concentration for the same control sample of purified lnC_2AB (black circles), and for the samples from peaks 1 (blue squares) and 2 (red triangles) of the gel filtration experiment shown in *A*. The experiments were performed in 25 mM Tris (pH 7.4) containing 125 mM NaCl and 1 mM Ca^{2+}. (*C*) UV spectra of samples corresponding to peaks 1 and 2 in the gel filtration chromatogram shown in *A*.

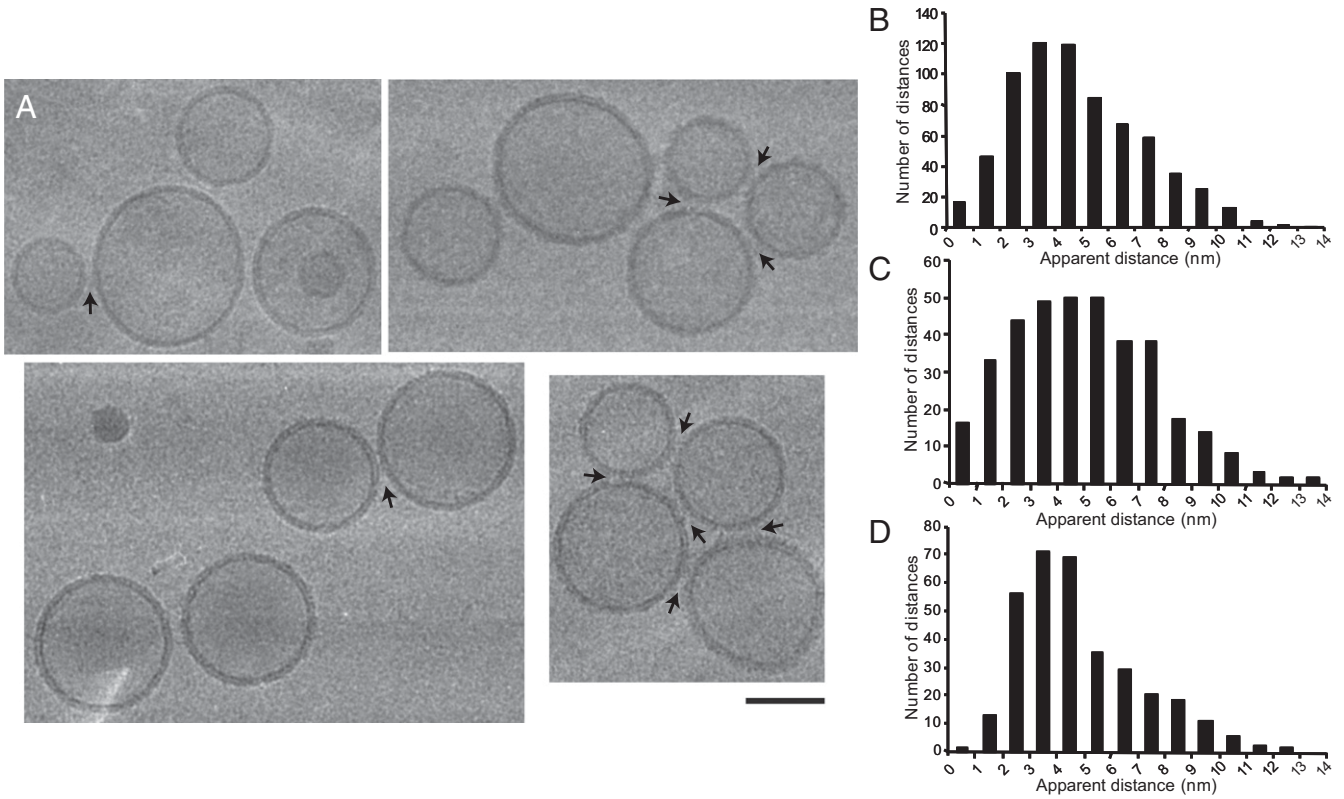

Fig. 4. Cryo-EM analysis of liposome clustering by lnC_2AB. Samples containing 3 μM or 10 μM lnC_2AB, 1 mM Ca^{2+}, and phospholipid vesicles (0.3 mg/mL lipids) were incubated and fast-frozen on EM grids (5 min after mixing the reagents). (*A*) Examples of the cryo-EM images obtained. Arrows indicate liposome pairs with apparent intermembrane distances of 4 nm or less. (Scale bar: 100 nm.) (*B*) Overall distribution of apparent distances measured between 697 selected liposome pairs bridged by lnC_2AB. (*C* and *D*) Distribution of apparent distances measured between liposome pairs in samples containing 3 μM lnC_2AB, yielding an lnC_2AB-to-lipid ratio of 1:120 (*C*), or 10 μM lnC_2AB, yielding an lnC_2AB-to-lipid ratio of 1:36 (*D*). The distribution of *B* includes all of the distances included in *C* and *D*. Note that protein-free liposomes do not cluster under the conditions of our experiments (20).

data were presented. In our images, we did observe a few instances of liposomes separated by distances of 8–10 nm that appeared to contain abundant electron density between the membranes, consistent with bridging by lnC_2AB oligomers or aggregates (see arrows in Fig. S3*A*). However, this type of interface was very rare. Indeed, the distances between apposed liposomes were generally smaller (Fig. 4 and Fig. S3*A*), and even in cases where the distances were ∼9 nm there was no clear density for lnC_2AB oligomers in most cases.

To have a representative quantitative picture of the distribution of distances between membranes bridged by lnC_2AB, we measured 697 apparent distances between pairs of liposomes. Because of the dynamic nature of liposome clustering, some of the vesicles were loosely clustered, with distances between vesicles that were clearly too long to involve bridging by lnC_2AB (Fig. S3*B*). Such long distances were not included in our measurements. The distribution of apparent intermembrane distances that we measured is centered on preponderant values of 3–4 nm with a smooth decay at longer values (Fig. 4*B*).

Because they provide 2D rather than 3D information, cryo-EM projection images tend to underestimate the intermembrane distance, particularly when there is a significant difference in vesicle size and when the distance is small. This problem is minimized by the fact that the vesicles are limited in their positional displacement because of the limited thickness of vitrified ice, usually less than 100 nm under our conditions as measured by burning a hole at a 45-degree tilt first and then visualizing it at −45 degree tilt (34). As a consequence, many specimen regions contained vesicles that were approximately in the same plane (Fig. 4 and Fig. S3*A*) (31). Thus, our measurements of intermembrane distances (Fig. 4*B*) focused on these regions and avoided areas where the ice was thick and included staggered vesicles. Because the underestimation of distances is expected to be smaller for pairs of larger vesicles, we also plotted the intermembrane distances for vesicle pairs where both vesicles had diameters of at least 70 nm (Fig. S4*A*). Although the distribution was less smooth because of the smaller numbers of distances included, it still resembled the overall distribution observed for all vesicle pairs (Fig. 4*B*). We estimated the error in our measurements and found that, in random sampling of the vertical displacement of the two vesicles, the averaged error of our measurement is less than 30% in the lower distance range and less than 10% in the longer range (Fig. S4 *B* and *C*).

We conclude that the histogram of Fig. 4*B* reflects reasonably well the actual intermembrane distances, with a bias at the shorter distances that shifts the center of the distribution slightly. Thus, though the preponderant distance values measured were 3–4 nm, the actual preponderant values are estimated to be 4–5 nm, which correspond to the size of a single C_2 domain oriented perpendicularly between the two membranes (Fig. 1*B*). These results parallel those obtained for C_2AB by cryoelectron tomography (20) and correspond to the distribution of intermembrane distances that can be expected if direct bridging constitutes the predominant mechanism of membrane bridging by lnC_2AB. Note that the observation of intermembrane distances longer than 5 nm, with a progressive decay in abundance as the distance increases, is a natural consequence of the dynamic nature of the vesicle clustering induced by lnC_2AB, with vesicles approaching before association or separating after

dissociation (as noted above for the results obtained with C_2AB in ref. 20).

This dynamic nature was further manifested by analyzing separately the distribution of intermembrane distances in the samples that had lnC_2AB-to-protein ratios of 1:120 or 1:36. For an lnC_2AB-to-protein ratio of 1:120, the distribution of intermembrane distances exhibited a maximum at 3–5 nm (Fig. 4*C*), and the profile was broader than the overall cumulative profile (Fig. 4*B*). In contrast, the maximum in the distribution of intermembrane distances was 3–4 nm for an lnC_2AB-to-protein ratio of 1:36 (Fig. 4*D*), and the relative abundance of the shorter distances was clearly higher than that observed at the lower protein-to-lipid ratio. These observations indicate that the higher protein density on the liposomes stabilizes the membrane–membrane bridging, keeping a higher percentage of interfaces at the molecular distance imposed by direct bridging, whereas the association–dissociation equilibrium is more dynamic at the lower protein densities, thus yielding a broader distribution of distances. It is important to note that, if both mechanisms (direct bridging and oligomerization) contribute substantially to liposome clustering, higher protein density would be expected to favor the oligomerization mechanism and hence to shift the maximum of the intermembrane distances to larger values, contrary to what we actually observed. Hence, these results not only show that direct bridging underlies the primary mechanism for membrane bridging by lnC_2AB, but also suggest that oligomerization does not contribute substantially to membrane bridging.

Contact of the Bottom of the C_2B Domain with the Membrane. NBD is an environment-sensitive probe that exhibits a large increase in fluorescence emission intensity when transferred from an aqueous to a hydrophobic environment (35). The increase in NBD fluorescence observed upon Ca^{2+}-dependent phospholipid binding of a mutant C_2AB (N396C) labeled with NBD at the bottom of the C_2B domain provided evidence that this bottom region contacts the membranes in a population of C_2AB molecules (20). In contrast, no increase in NBD fluorescence was observed in similar experiments performed with NBD-labeled N396C mutant lnC_2AB (29). To test in our own hands whether this discrepancy arose from the use of different synaptotagmin-1 fragments, we performed analogous experiments, side by side with NBD-labeled N396C mutant C_2AB and lnC_2AB samples and the same liposome preparations. We observed similar increases in NBD fluorescence for both C_2AB and lnC_2AB upon Ca^{2+}-dependent phospholipid binding (Fig. 5 *A*, *B*, and *E*). These results are comparable to those we obtained previously for C_2AB with liposomes containing a higher percentage (30%) of phosphatidylserine (PS) (20), and were reproducible in a large number of experiments that we performed in different days with different preparations. The experiments were performed with protein-to-lipid ratios that lead to liposome clustering, which we verified using dynamic light-scattering (DLS) (20), but analogous NBD fluorescence increases were observed under conditions where clustering does not occur (Fig. 5 *C*–*E*). Hence, these increases reflect an intrinsic tendency of the bottom of the C_2B domain to bind to membranes even in the absence of clustering. Note also that the finding that the increase in NBD fluorescence is not larger under clustering conditions is not surprising because only a small percentage of the C_2AB molecules that cover the vesicle surface can participate in clustering, given the dynamic nature of clustering and the fact that only small regions of the vesicle surfaces are apposed to other vesicles upon clustering.

The NBD fluorescence increases that we observed are modest, which could arise from an interfacial location of the NBD probe in a majority of molecules or from a small population that has a large fluorescence increase. However, we favor the second possibility because a large amount of evidence showed that a majority of C_2AB molecules bind to membranes primarily through the Ca^{2+}-binding loops at the top of both C_2 domains (15–17, 36), and the bottom of the C_2B domain by itself is not sufficient for lipid binding (20). Indeed, NBD probes placed at the tip of the Ca^{2+}-binding loops exhibit much larger increases in fluorescence upon membrane binding than those observed with the probe at the bottom of the C_2B domain (20). We estimate that the population of molecules where the bottom of the C_2B domain contacts the membrane is at least 5–10%, assuming that NBD probes placed at the bottom or the top loops undergo comparable fluorescence emission increases upon membrane binding, but the population would be larger if NBD probes placed at the bottom of the C_2B domain undergo lower fluorescence increases because of an interfacial location.

Substantial Populations of Antiparallel Orientations of the Two C_2 Domains on Nanodiscs. Because the Ca^{2+}-binding loops at the top of the C_2A domain are involved in membrane binding for a majority of C_2AB molecules, and the NBD fluorescence data

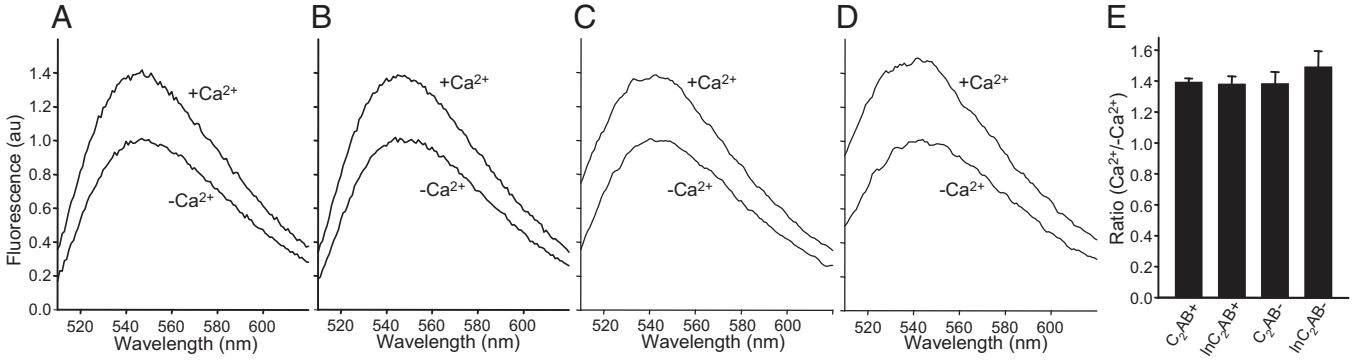

Fig. 5. Increased fluorescence of NBD probes placed at the bottom of the C_2B domain upon membrane binding. (*A* and *B*) Representative fluorescence emission spectra of 0.3-μM samples of NBD-labeled N396C mutant C_2AB (*A*) or lnC_2AB (*B*) acquired side by side in the presence of phospholipid vesicles (100-μM lipids) and 1 mM EGTA or 1 mM Ca^{2+} (clustering conditions). (*C* and *D*) Analogous spectra acquired under the same conditions but using 1-mM lipids (nonclustering conditions). For each set of experiments in *A*–*D*, spectra acquired with identical samples containing unlabeled C_2AB or lnC_2AB were subtracted to remove contributions from light scattering to the observed intensities. The data were then normalized to the maximum fluorescence intensity observed in the absence of Ca^{2+}. (*E*) Quantification of NBD fluorescence increases upon membrane binding. NBD fluorescence emission spectra analogous to those shown in *A*–*D* were acquired in triplicate under clustering conditions (C_2AB+ and lnC_2AB+) or nonclustering conditions (C_2AB- and lnC_2AB-). Bars represent averages of the ratios between the NBD fluorescence intensity maxima observed in 1 mM Ca^{2+} and 1 mM EGTA in three separate pairs of experiments performed under identical conditions. Error bars represent SDs.

show that a small but sizeable population of molecules bind to a single membrane through the bottom of the C_2B domain, this population of molecules is expected to involve conformations with an antiparallel arrangement of the two C_2 domains. This notion agrees with an EPR study that measured distances between pairs of spin labels placed at the two domains of lnC_2AB (24), although distances between the top of one domain and the bottom of the other were not measured. To obtain direct evidence for proximity between the opposite ends of the C_2A and C_2B domain on a membrane, we performed an NMR analysis of C_2AB bound to nanodiscs, which are disk-like phospholipid bilayers surrounded by a scaffolding protein (37). For this purpose, we used perdeuterated C_2AB specifically $^{1}H,^{13}C$-labeled at Ile, Leu, and Val methyl groups (^{2}H-ILV-$^{13}CH_3$-C_2AB) and took advantage of the high sensitivity of ^{1}H-^{13}C heteronuclear multiple-quantum coherence (HMQC) spectra of proteins labeled with this scheme even for large protein complexes (38).

The cross-peaks from the ^{1}H-^{13}C HMQC spectrum of ^{2}H-ILV-$^{13}CH_3$-C_2AB in the presence of nanodiscs containing 15% dioleoyl-PS (DOPS) and 1 mM Ca^{2+} are considerably broader than those of Ca^{2+}-free ^{2}H-ILV-$^{13}CH_3$-C_2AB (Fig. S5 *A* and *B*), but they are still observable with high sensitivity. Comparison of ^{1}H-^{13}C HMQC spectra of isolated ^{2}H-ILV-$^{13}CH_3$-C_2AB in the presence of 0, 1, and 20 mM Ca^{2+} revealed progressive changes in cross-peaks from methyl groups in the Ca^{2+}-binding loops, similar to the behavior observed for amide groups (14), and these cross-peaks exhibited some additional movements in spectra acquired in the presence of nanodiscs and 1 mM Ca^{2+} (Fig. S5*C*). These results show that ^{2}H-ILV-$^{13}CH_3$-C_2AB is fully bound to the nanodiscs under the conditions of our experiments and that the observed cross-peaks do not arise from residual unbound ^{2}H-ILV-$^{13}CH_3$-C_2AB. DLS experiments showed that C_2AB-mediated bridging of nanodiscs does not occur under the conditions of these experiments, and hence that NMR data acquired under these conditions should reflect the conformational distribution of C_2AB molecules bound to a single membrane.

To gain insight into the relative orientations of the two domains, we prepared ^{2}H-ILV-$^{13}CH_3$-C_2AB single mutants where either N248 at the bottom of the C_2A domain or V304 at the top of the C_2B domain were replaced by a cysteine and labeled with the paramagnetic probe (1-oxyl-2,2,5,5-tetramethyl-3-pyrroline-3-methyl)methanethiosulfonate (MTSL). ^{1}H-^{13}C HMQC spectra of the ^{2}H-ILV-$^{13}CH_3$-C_2AB mutants bound to nanodiscs before and after reduction of the probe allowed us to measure paramagnetic broadening effects (PBEs; defined as the ratios between the cross-peak intensities before and after reduction) (39).

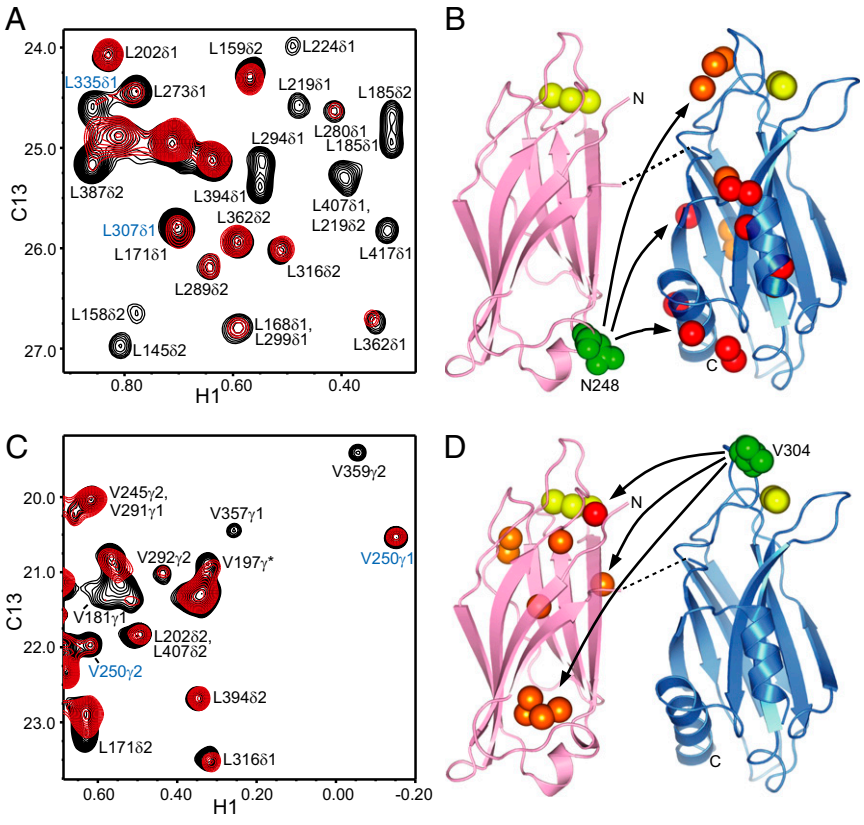

Fig. 6. Analysis of PBEs within C_2AB bound to nanodiscs. (*A* and *C*) ^{1}H-^{13}C HMQC spectra of 50-μM MTSL-labeled ^{2}H-ILV-$^{13}CH_3$-C_2AB N248C (*A*) or V304C (*C*) mutant in the presence of 1-mM Ca^{2+} and 60-μM nanodiscs before (red) or after (black) reduction with 1 mM dithionite and 1 mM ascorbic acid. Assignments based on our previous NMR studies of the isolated C_2A and C_2B domains (15, 40) are indicated for well-resolved cross-peaks. Cross-peaks from methyl groups that exhibit PBEs indicative of antiparallel orientations of the C_2 domains (at the top of the C_2B domain in *A* and to the bottom of the C_2A domain in *C*) are labeled in blue. (*B* and *D*) Summary of the interdomain PBEs measured for the N248C (*B*) or V304C (*D*) mutant. Ribbon diagrams of the C_2A (*Left*) and C_2B (*Right*) domains are shown, with the Ca^{2+} ions shown as yellow spheres and the atoms of the residues that were mutated to place the MTSL labels shown as green spheres. The methyl carbons that exhibited strong (0–0.4) or medium (0.4–0.6) interdomain PBEs are shown as red or orange spheres, respectively. The residues bearing these methyl groups are 294, 387, 394, 401, 409, 413, and 417 (red) and 273, 291, 292, 307, and 335 (orange) in *B*; 171 (red) and 149, 158, 181, 197, 239, 240, and 250 (orange) in *D*. The curved arrows are meant to illustrate that the MTSL label placed at the bottom of the C_2A domain (N248C) induces substantial PBEs in the bottom, middle, and top of the C_2B domain, whereas the MTSL label placed at the top of the C_2B domain (V304C) induces substantial PBEs at the top, middle, and bottom of the C_2A domain. The dashed lines represent the linker between the C_2A and C_2B domains.

The intradomain PBEs observed for the cross-peaks of the C_2A domain in the N248C mutant and for the cross-peaks of the C_2B domain in the V304C mutant (Fig. 6) followed the expected r^{-6} dependence (where r is the distance between the corresponding methyl group and the probe) according to the known 3D structures of the domains (13, 15, 40).

The observation of interdomain PBEs in multiple regions of the C_2B domain for the N248C mutant and in multiple regions of the C_2A domain for the V304C mutant is consistent with EPR (24), and single-molecule FRET (41, 42) studies that revealed a dynamic relative orientation between the two domains. For the N248C mutant that contained the MTSL probe at the bottom of the C_2A domain, we observed some strong PBEs (<0.4) and medium PBEs (= 0.4–0.6) for multiple cross-peaks at the bottom and middle of the C_2B domain (Fig. 6 *A* and *B*), indicating a predominance of parallel and oblique orientations of the two C_2 domains. Note that both types of orientations can allow simultaneous binding of the Ca^{2+}-binding loops from both domains to the same membrane, and that there likely is a continuum of relative orientations that allow such simultaneous binding. Hence, these results are consistent with the expected prevalence of C_2AB molecules that bind to a membrane via the top loops of both domains. However, we also observed medium PBEs between the MTSL probe at the bottom of the C_2A domain and methyl groups in the top of the C_2B domain (Fig. 6 *A* and *B*), which must originate from conformations with an antiparallel orientation of the two domains. The interdomain PBEs observed for the V304C mutant with the MTSL probe at the top of the C_2B domain were generally weaker than those observed for the N248C mutant, with only one strong PBE that involved a methyl group at the top of the C_2A domain. This result likely arises because residue 304 is at the very tip of a top loop of the C_2B domain and hence is not very close to methyl groups of the C_2A domain in most available conformations. Nevertheless, we did observe medium PBEs with several methyl groups from the top, middle, and bottom of the C_2A domain (Fig. 6 *C* and *D*), consistent with the conclusions drawn from the analysis with the N248C mutant and confirming again the existence of a population of C_2AB molecules bound to a membrane with an antiparallel orientation of the two C_2 domains. It is not feasible to reliably quantify this population from the measured PBEs because of the highly dynamic nature of this system, but the overall results are fully consistent with the population of molecules where the bottom of the C_2B domain contacts the membrane estimated from the NBD fluorescence data.

Discussion

The observation that synaptotagmin-1 can aggregate chromaffin granules and liposomes (19), and that Ca^{2+}-bound C_2AB can bridge two membranes to bring them within 4 nm, led to an attractive model whereby synaptotagmin-1 triggers synaptic vesicle fusion by bringing the vesicle and plasma membranes into close proximity in a Ca^{2+}-dependent manner, in cooperation with the SNAREs (20). This model was supported by the finding that Ca^{2+}-evoked neurotransmitter release is almost completely abolished by a mutation of two arginines at the bottom of the C_2B domain that impairs the liposome clustering activity of C_2AB and its ability to stimulate SNARE-dependent lipid mixing between liposomes (7). However, an alternative model proposed that lnC_2AB oligomerization is required for its membrane bridging activity and that such activity involves protein–protein interactions between lnC_2AB molecules bound to the two apposed membranes, with no contact of the bottom of the C_2B domain with the membranes (29). This model was supported by cryo-EM images reported in a separate study (25). Assessing the validity of these two models and clarifying the apparently contradictory data from different studies is critical to understand how synaptotagmin-1 triggers neurotransmitter release. The data presented here show that direct bridging constitutes the primary mechanism by which both C_2AB and lnC_2AB bring two membranes into apposition, and that the bottom of the C_2B domain in a fraction of C_2AB and lnC_2AB molecules contacts the membranes even in the absence of membrane bridging.

We would like to emphasize that, so far, no evidence has been provided to support the oligomerization mechanism for the shorter C_2AB fragment. On the contrary, our NMR data (20, 23) (Fig. S1) demonstrate that C_2AB has no detectable tendency to self-associate in solution even at high protein and Ca^{2+} concentrations. Moreover, no cross-linking of C_2AB bound to liposomes was induced by the highly efficient agent Tris(bipyridine)ruthenium(II) (20) despite the very high local concentrations of C_2AB molecules on the membranes, and FRET experiments provided additional compelling data showing that C_2AB does not oligomerize on membranes (20). Finally, cryo-EM images showed that the distances between vesicle pairs bridged by C_2AB are predominantly ~4 nm (20), which is incompatible with the oligomerization model and can only be explained by direct membrane bridging by C_2AB. Because the activity of C_2AB in stimulating SNARE-dependent lipid mixing between liposomes in reconstitution experiments (7) is comparable to that of lnC_2AB (43), all these observations clearly establish that oligomerization is not required for this stimulatory activity.

EPR studies also yielded strong support for the direct bridging model for lnC_2AB (24), and no oligomerization of lnC_2AB under membrane bridging conditions was observed by EPR (24) or fluorescence spectroscopy (44). The study that proposed the oligomerization model using lnC_2AB (29) did not account for the EPR data or the results that were already available for C_2AB (20); relied on the cryo-EM images of a separate study (25); and supported the model with a series of indirect experiments, without providing direct evidence for the existence of protein–protein interactions that help to bridge the membranes. In our cryo-EM analysis with lnC_2AB (Fig. 4 and Fig. S3), we did not observe the extended parallel surfaces of liposomes with clear protein density between them and a separation of 9 nm reported previously (25). Because no statistical analysis of the prevalence of these extended surfaces was described, it is unclear to what extent the cryo-EM data from this previous study are contradictory with our results. Our analysis of 697 vesicle–vesicle interfaces reveals that apparent intermembrane distances of 3–4 nm (actual distances of 4–5 nm) predominate, thus showing that a majority of lnC_2AB molecules bring membranes together by direct bridging. We did observe some interfaces with intermembrane distances of 8–10 nm and accumulation of electron density that might correspond to lnC_2AB oligomers. However, this type of interface was very rare (less than 1%) and might arise from nonspecific aggregates of lnC_2AB caused by the presence of residual polyacidic contaminants in a small percentage of lnC_2AB molecules, rather than from well-defined lnC_2AB oligomers. In this context, it is worth noting that properly purified lnC_2AB has no tendency to aggregate in solution in 1 mM Ca^{2+} even at 100-μM protein concentration, but the presence of such contaminants does lead to aggregation at protein concentrations above 10 μM (Fig. 3).

The study that proposed the oligomerization model used lnC_2AB samples that aggregate at more than 10 μM concentration (29). Moreover, the primary evidence provided to conclude that membrane bridging requires *trans* interactions between lnC_2AB molecules bound to separate membranes relied on the finding that immobilized liposomes containing prebound lnC_2AB pulled down target liposomes containing prebound lnC_2AB, but not free liposomes (29). Interpretation of these data assumed that the prebound lnC_2AB molecules were permanently pinned to their respective liposomes because of their very slow dissociation rates, as described in ref. 45. However, the rates reported in that reference are on the order of 10 s^{-1}. Hence, lnC_2AB should readily redistribute among liposome populations in the

time scale of the pull-down assays, and the lack of binding of the target plain liposomes can be attributed merely to the overall decrease in lnC_2AB concentration, which resulted in protein-to-lipid ratios that do not support liposome clustering (figure 3 in ref. 29). Furthermore, direct membrane bridging by lnC_2AB was presumably ruled out by the lack of an increase in fluorescence for NBD probes placed at the bottom of the C_2B domain (including residue 396) upon membrane binding, and by the absence of FRET between these probes and rhodamine-labeled lipids (29). However, interpretation of these data are hindered by the fact that only a small percentage of membrane-bound lnC_2AB molecules is expected to contribute to bridging to other membranes (see above), and the effects of clustering on NBD fluorescence are thus expected to be very small, likely within the error of the measurements. Note also that we do see a fluorescence increase for an NBD probe placed at residue 396 upon membrane binding for both lnC_2AB and C_2AB (Fig. 5) (20). It is unclear why such increase was not observed for the lnC_2AB 396 mutant in ref. 29, but it is tempting to speculate that it may arise from insufficient purification of the lnC_2AB 396 mutant in that study, given the aggregation reported for the WT lnC_2AB (29).

The modest nature of the increases in fluorescence that we observe for NBD probes at the bottom of the C_2B domain upon Ca^{2+}-dependent binding of C_2AB or lnC_2AB to membranes (Fig. 5), together with the much larger increases observed with NBD probes at the Ca^{2+}-binding loops (20) and the analysis of PBEs in C_2AB bound to nanodiscs (Fig. 6), suggest that a majority of molecules bind to a single membrane through the Ca^{2+}-binding loops of both C_2 domains. It is important to realize that this feature arises naturally from the high membrane-affinity of the Ca^{2+}-binding loops and is fully compatible with the direct bridging model. Moreover, only a small percentage of molecules needs to bind to an apposed membrane via the bottom of the C_2B domain to mediate direct bridging, which could occur in both parallel and antiparallel orientations of the domains (Fig. 1*B*). The NBD data also show that a population of molecules binds to membranes with an antiparallel orientation of the C_2 domains and the bottom of the C_2B domain contacting the membrane. We estimate that this population is at least 5–10% based on the observed NBD increases, but it could be considerably higher if the NBD probes at the bottom of the C_2B domain contact the membrane at an interfacial position, whereas those at the Ca^{2+}-binding loops insert more deeply into the bilayer. This overall picture is consistent with our PBE measurements on nanodiscs, as well as with EPR data obtained with lnC_2AB that revealed proximity of the bottom of the C_2B domain to the membrane surface and a substantial population of molecules with antiparallel orientations (24). Although the EPR analysis suggested a predominance of antiparallel orientations, the EPR and NBD data are not necessarily inconsistent given the uncertainties in the populations that can be estimated by either method. Regardless of these uncertainties, the NBD, PBE, and EPR data leave no doubt that a sizeable population of C_2AB/lnC_2AB molecules bind to membranes with an antiparallel orientation of the C_2 domains.

In summary, we cannot completely rule out that a small population of lnC_2AB molecules form well-defined oligomers between membranes, but there is currently no clear evidence for the existence of such well-defined oligomers, and the rare occurrences of lnC_2AB aggregates between membranes that appear to be visible in our cryo-EM images could be induced by the presence of residual amounts of polyacidic contaminants, much like these contaminants promote aggregation in solution. Moreover, there is very compelling data against oligomerization for C_2AB bound to membranes (20), and the results presented here, together with previously available data (20), provide overwhelmingly evidence supporting the notion that the synaptotagmin-1 C_2 domains bring membranes into apposition primarily by the direct bridging mechanism. One could argue that all these data were obtained in vitro and that high local concentrations of synaptotagmin-1 between a docked synaptic vesicle and the plasma membrane could favor oligomerization in vivo. However, synaptic vesicles contain on average 15 synaptotagmin-1 molecules (46), whereas no oligomerization was observed for membrane-bound C_2AB under conditions where the protein density on the membranes was threefold higher (20). Furthermore, mechanistic considerations also favor the bridging model because a synaptotagmin-1 oligomer between the membranes would be expected to hinder rather than promote membrane fusion, whereas single synaptotagmin-1 molecules could readily diffuse away from the center of the intermembrane space to bind to the SNAREs and cooperate with them in bringing the synaptic vesicle and plasma membranes together by the direct bridging mechanism (23) (Fig. S6). Nevertheless, a better understanding of the nature of synaptotagmin-1–SNARE interactions and additional correlations between the clustering abilities of synaptotagmin-1 mutants and their functional activities in vivo, beyond that already established (7), will be required to further investigate the validity of the direct bridging mechanism.

Materials and Methods

Recombinant Proteins. N-terminal GST fusion proteins of synaptotagmin fragments 140–421 (C_2AB) and 95–421(lnC_2AB) were expressed in *Escherichia coli* BL21(DE3) cells and purified as previously described (20, 32), with slight modifications. Briefly, the proteins were expressed in Lennox L Broth media at 25 °C for 18 h with 0.4 mM isopropyl β-D-1-thiogalactopyranoside. Cells were resuspended in buffer A [40 mM Tris·HCl (pH 8.2), 200 mM NaCl, 2 mM DTT] with 1% Triton and protease inhibitor mixture, and lysed using an Avestin EmulsiFlex-C5 homogenizer. The soluble fraction of the cell lysate was collected after centrifugation at 48,000 × *g* for 30 min and incubated with Glutathione Sepharose 4B (GE Healthcare) at 4 °C for 12 h. The resin was washed with buffer A, buffer A + 50 mM $CaCl_2$, and buffer A + 50 mM $CaCl_2$ + 1 M NaCl. Remaining nucleic acid contaminants bound to synaptotagmin fragments were then cleared with benzonase treatment (40 units per milliliter of solution, corresponding to ∼1,000 units per liter of cell culture) in 50 mM Tris (pH 8.0), 2 mM $MgCl_2$ for 2 h at room temperature with gentle rotation of the beads. The GST tag was cleaved with thrombin on the resin at room temperature for 3 h. Synaptotagmin fragments were further purified with an ion exchange Source S column [buffers: 50 mM NaAc (pH 6.2), 5 mM $CaCl_2$; and 50 mM NaAc (pH 6.2), 5 mM $CaCl_2$, 1 M NaCl] and size-exclusion chromatography on a Superdex 75 16/60 column using 25 mM Tris (pH 7.4) containing 125 mM NaCl as the buffer.

Synaptotagmin C277S and N396C double mutations for both C_2AB and lnC_2AB were generated by the QuikChange site-directed mutagenesis kit (Stratagene). The proteins were labeled with *N*,*N*′-dimethyl-*N*-(iodoacetyl)-*N*′-(7-nitrobenz-2-oxa-1,3-diazol-4-yl)ethylenediamine (IANBD amide) (Invitrogen) according to manufacturer's protocol using 50–60 μM of syantotagmin-1 fragments and 400 μM IANBD amide in the presence of 100 μM Tris (2-carboxyethyl)phosphine at room temperature with 2-h incubation time. All of the experiments were performed in 25 mM Hepes (pH 7.4), 150 mM KCl, and 1 mM $MgCl_2$ reconstitution buffer unless otherwise indicated.

Preparation of Phospholipid Vesicles. The 1,2-dioleoyl-*sn*-glycero-3-[phospho-L-serine] (DOPS), 1-palmitoyl-2-oleoyl-*sn*-glycero-3-phosphocholine (POPC), and 1-palmitoyl-2-oleoyl-*sn*-glycero-3-phosphoethanolamine (Avanti Polar Lipids) in chloroform were mixed in a glass test tube in a desired ratio, and chloroform was evaporated using dry nitrogen stream. The lipids were placed in a vacuum chamber overnight for complete removal of organic solvent. Lipid films were hydrated with reconstitution buffer in an appropriate volume yielding 10 mM lipids. Lipids were vortexed >5 min then frozen and thawed five times. Large unilamellar vesicles were prepared by extruding the hydrated lipid solution through 0.08-μm polycarbonate membranes 23 times using an Avanti Mini-Extruder. The homogeneity of the vesicle size distribution was confirmed by dynamic light scattering and cryo-EM, and was centered around a diameter of 80 nm.

Fluorescence Experiments. NBD fluorescence emission (500–620 nm) experiments were performed on a Photon Technology International spectrophotometer with a 4-nm slit width and 485-nm excitation at room temperature using 0.3-μM synaptotagmin-1 fragments and 0.1- or 1-mM lipid vesicles

(DOPS:POPC:POPC 15:55:30) in reconstitution buffer including 1 mM EGTA or 1 mM $CaCl_2$. Experiments under all of the conditions were repeated at least three times, and SDs were calculated. All of the experiments were repeated with unlabeled synaptotagmin fragments, and the data were subtracted from actual data as background. Microsquare cuvettes with 5-mm interior width and 400-μL volume capacity were used to obtain reliable data. Cuvettes with lower volume capacity (e.g., submicrocuvettes) gave considerably more variability in the data.

Turbidity. Aggregation of differentially purified synaptotagmin-1 lnC_2AB fragments was monitored from the absorbance at 400 nm using a Varioskan Flash Plate Reader on a clear-bottom black 96-well plate. Experiments were performed in 25 mM Tris (pH 7.4) containing 125 mM NaCl, 1 mM Ca^{2+}, and the indicated protein concentrations.

Cryo-EM. Both sides of Quantifoil 200 mesh copper, R2/2 hole shape, 2 μm hole size and 4 μm period grids were glow-discharged in a Denton Vacuum DV-502A instrument with 40-mA current for 45 s. Whatman paper with a 0.2-mL drop of amylamine was prepared immediately before use and included during the glow discharge to prevent extensive binding of liposomes onto the carbon surface of the grid. Samples for cryo-EM were prepared by incubating 0.3 mg/mL lipid vesicles (DOPS:POPC 20:80) with 3 μM or 10 μM lnC_2AB fragment (resulting in protein to lipid ratios of 1:120 or 1:36, respectively) in reconstitution buffer at room temperature for 2 min; 3 μL of the sample were loaded onto the carbon side of a Quantifoil grid, incubated for 10 s, and blotted with a piece of Whatman no. 4 paper from the edge of the grid for 5 s. Another 3 μL of the sample were loaded onto the same side of the grid and rapidly frozen using Vitrobot FP 5350/60-type automated vitrification robot. The total incubation time up to the blotting step was ~5 min. The blotting time was 2 s and the humidity in the blotting chamber was above 95%. Standard Vitrobot Filter paper, Ø55/20 mm, grade 595, was used for blotting. Images were taken with a JEOL 2200FS transmission electron microscope equipped with an energy filter at cryotemperatures, keeping samples on an Oxford Instruments cryoholder. Images were taken at 52.95 K calibrated magnification and were recorded on a 2K × 2K Tietz slow scan CCD camera or Kodak SO-163–type films. The electron density was kept at 20–30 electrons per square angstrom during each exposure by a minimum dosage system. Films were scanned with a PhotoScan Instrument from Z/I Imaging at 14-μm resolution. Measurements of distances between membranes were performed using ImageJ.

Nanodisc Preparation. Nanodiscs were prepared as previously described (47) with small modifications (48). Briefly, ApoA1 and lipids (DOPS:POPC 15:85) at an ApoA1:lipid ratio of 2:130 were mixed with 1% n-octyl-β-D-glucopyranoside and 1% sodium cholate. The mixture was vortexed and then incubated at room temperature for 30 min. The nanodiscs were formed by passing the mixture over a 4-cm-high column of Extracti-Gel D resin (Pierce) to remove the detergent. The nanodiscs were then purified on a Superdex-200 HiLoad 16/60 column (GE Healthcare) in 25 mM Tris·HCl (pH 7.4), 125 mM NaCl, 1 mM $CaCl_2$, concentrated using a 30-kDa molecular weight cutoff filter, and exchanged to the same buffer in 100% D_2O.

Spin Labeling of Syt1. To prepare the ^{2}H-ILV-$^{13}CH_3$-C_2AB N248C or V304C mutants for spin labeling, they were first treated with 10 mM DTT, and the DTT was then removed by cation exchange chromatography on Source S. The final buffer composition after cation exchange was ~50 mM sodium acetate (NaOAc), pH 6.2, 400 mM NaCl, 5 mM $CaCl_2$. The protein was concentrated to 40–60 μM and a 10-fold excess of MTSL was added from a 40-mM stock in dimethyl sulfoxide. The mixture was rotated overnight at 4 °C to allow complete cysteine labeling; the excess MTSL was removed by buffer exchange in 25 mM Tris·HCl (pH 7.4), 125 mM NaCl, 1 mM $CaCl_2$ using a 10-kDa molecular weight cutoff filter; and the sample was exchanged to the same buffer in 100% D_2O. The paramagnetic activity of MTSL was removed by reduction with 1 mM sodium dithionite and 1 mM ascorbic acid from 100-mM stocks. The dithionite stocks were prepared immediately before addition (<30 min) due to its high instability.

NMR Spectroscopy. NMR spectra were acquired at 25 °C on Varian INOVA800 or INOVA600 spectrometers. ^{1}H-^{15}N HSQC and ^{1}H-^{13}C HMQC spectra were acquired under the conditions indicated in the figure legends using H_2O/D_2O 95:5 (vol/vol) or 100% D_2O, respectively, as the solvent. Total acquisition times were 2–12 h. NMR data were processed with NMRPipe (49) and analyzed with NMRView (50).

ACKNOWLEDGMENTS. We thank Bazbek Davletov for providing a sample of lnC_2AB protein and a vector to express lnC_2AB in bacteria, Sourabh Banerjee and Thomas Sakmar for advice on preparation of nanodiscs, and Amy Zhou for fruitful discussions. This work was supported by Welch Foundation Grants I-1304 (to J.R.) and I-1684 (to Q.-X.J.), Cancer Prevention Research Institute of Texas Grant RP120474 (to Q.-X.J.), and National Institutes of Health (NIH) Grants NS40944 (to J.R.) and GM088745 and GM093271 (to Q.-X.J.). K.D.B. was supported in part by NIH Training Grant T32 GM008297.

1. Rizo J, Südhof TC (2012) The membrane fusion enigma: SNAREs, Sec1/Munc18 proteins, and their accomplices—guilty as charged? *Annu Rev Cell Dev Biol* 28: 279–308.
2. Jahn R, Fasshauer D (2012) Molecular machines governing exocytosis of synaptic vesicles. *Nature* 490(7419):201–207.
3. Brunger AT, Weninger K, Bowen M, Chu S (2009) Single-molecule studies of the neuronal SNARE fusion machinery. *Annu Rev Biochem* 78:903–928.
4. Chapman ER (2008) How does synaptotagmin trigger neurotransmitter release? *Annu Rev Biochem* 77:615–641.
5. Fernández-Chacón R, et al. (2001) Synaptotagmin I functions as a calcium regulator of release probability. *Nature* 410(6824):41–49.
6. Bhalla A, Chicka MC, Tucker WC, Chapman ER (2006) Ca(2+)-synaptotagmin directly regulates t-SNARE function during reconstituted membrane fusion. *Nat Struct Mol Biol* 13(4):323–330.
7. Xue M, Ma C, Craig TK, Rosenmund C, Rizo J (2008) The Janus-faced nature of the C(2)Bdomain is fundamental for synaptotagmin-1 function. *Nat Struct Mol Biol* 15(11):1160–1168.
8. Schaub JR, Lu X, Doneske B, Shin YK, McNew JA (2006) Hemifusion arrest by complexin is relieved by Ca2+-synaptotagmin I. *Nat Struct Mol Biol* 13(8):748–750.
9. Tang J, et al. (2006) A complexin/synaptotagmin 1 switch controls fast synaptic vesicle exocytosis. *Cell* 126(6):1175–1187.
10. Giraudo CG, Eng WS, Melia TJ, Rothman JE (2006) A clamping mechanism involved in SNARE-dependent exocytosis. *Science* 313(5787):676–680.
11. Parisotto D, Malsam J, Scheutzow A, Krause JM, Söllner TH (2012) SNAREpin assembly by Munc18-1 requires previous vesicle docking by synaptotagmin 1. *J Biol Chem* 287(37):31041–31049.
12. Ma C, Su L, Seven AB, Xu Y, Rizo J (2013) Reconstitution of the vital functions of Munc18 and Munc13 in neurotransmitter release. *Science* 339(6118):421–425.
13. Sutton RB, Davletov BA, Berghuis AM, Südhof TC, Sprang SR (1995) Structure of the first C2 domain of synaptotagmin I: A novel Ca2+/phospholipid-binding fold. *Cell* 80(6):929–938.
14. Ubach J, Zhang X, Shao X, Südhof TC, Rizo J (1998) Ca2+ binding to synaptotagmin: How many Ca2+ ions bind to the tip of a C2-domain? *EMBO J* 17(14):3921–3930.
15. Fernandez I, et al. (2001) Three-dimensional structure of the synaptotagmin 1 C2B-domain: Synaptotagmin 1 as a phospholipid binding machine. *Neuron* 32(6): 1057–1069.
16. Chapman ER, Davis AF (1998) Direct interaction of a Ca2+-binding loop of synaptotagmin with lipid bilayers. *J Biol Chem* 273(22):13995–14001.
17. Zhang X, Rizo J, Südhof TC (1998) Mechanism of phospholipid binding by the C2A-domain of synaptotagmin I. *Biochemistry* 37(36):12395–12403.
18. Rhee JS, et al. (2005) Augmenting neurotransmitter release by enhancing the apparent Ca2+ affinity of synaptotagmin 1. *Proc Natl Acad Sci USA* 102(51): 18664–18669.
19. Damer CK, Creutz CE (1994) Synergistic membrane interactions of the two C2 domains of synaptotagmin. *J Biol Chem* 269(49):31115–31123.
20. Araç D, et al. (2006) Close membrane-membrane proximity induced by Ca(2+)-dependent multivalent binding of synaptotagmin-1 to phospholipids. *Nat Struct Mol Biol* 13(3):209–217.
21. Mackler JM, Drummond JA, Loewen CA, Robinson IM, Reist NE (2002) The C(2)B Ca(2+)-binding motif of synaptotagmin is required for synaptic transmission in vivo. *Nature* 418(6895):340–344.
22. Robinson IM, Ranjan R, Schwarz TL (2002) Synaptotagmins I and IV promote transmitter release independently of Ca(2+) binding in the C(2)A domain. *Nature* 418(6895):336–340.
23. Dai H, Shen N, Araç D, Rizo J (2007) A quaternary SNARE-synaptotagmin-Ca2+-phospholipid complex in neurotransmitter release. *J Mol Biol* 367(3):848–863.
24. Herrick DZ, et al. (2009) Solution and membrane-bound conformations of the tandem C2A and C2B domains of synaptotagmin 1: Evidence for bilayer bridging. *J Mol Biol* 390(5):913–923.
25. Connell E, et al. (2008) Cross-linking of phospholipid membranes is a conserved property of calcium-sensitive synaptotagmins. *J Mol Biol* 380(1):42–50.
26. van den Bogaart G, et al. (2011) Synaptotagmin-1 may be a distance regulator acting upstream of SNARE nucleation. *Nat Struct Mol Biol* 18(7):805–812.
27. Park Y, et al. (2012) Controlling synaptotagmin activity by electrostatic screening. *Nat Struct Mol Biol* 19(10):991–997.
28. Vennekate W, et al. (2012) *Cis*- and *trans*-membrane interactions of synaptotagmin-1. *Proc Natl Acad Sci USA* 109(27):11037–11042.
29. Hui E, et al. (2011) Mechanism and function of synaptotagmin-mediated membrane apposition. *Nat Struct Mol Biol* 18(7):813–821.
30. Diao J, Yoon TY, Su Z, Shin YK, Ha T (2009) C2AB: A molecular glue for lipid vesicles with a negatively charged surface. *Langmuir* 25(13):7177–7180.
31. Diao J, et al. (2012) Synaptic proteins promote calcium-triggered fast transition from point contact to full fusion. *elife* 1:e00109.

32. Ubach J, et al. (2001) The C2B domain of synaptotagmin I is a Ca2+-binding module. *Biochemistry* 40(20):5854–5860.
33. Zhou A, Brewer KD, Rizo J (2013) Analysis of SNARE complex/synaptotagmin-1 interactions by one-dimensional NMR spectroscopy. *Biochemistry* 52(20):3446–3456.
34. Sun J, Li H (2010) How to operate a cryo-electron microscope. *Methods Enzymol* 481: 231–249.
35. Crowley KS, Reinhart GD, Johnson AE (1993) The signal sequence moves through a ribosomal tunnel into a noncytoplasmic aqueous environment at the ER membrane early in translocation. *Cell* 73(6):1101–1115.
36. Wu Y, et al. (2003) Visualization of synaptotagmin I oligomers assembled onto lipid monolayers. *Proc Natl Acad Sci USA* 100(4):2082–2087.
37. Denisov IG, Grinkova YV, Lazarides AA, Sligar SG (2004) Directed self-assembly of monodisperse phospholipid bilayer nanodiscs with controlled size. *J Am Chem Soc* 126(11):3477–3487.
38. Ruschak AM, Kay LE (2010) Methyl groups as probes of supra-molecular structure, dynamics and function. *J Biomol NMR* 46(1):75–87.
39. Clore GM, Iwahara J (2009) Theory, practice, and applications of paramagnetic relaxation enhancement for the characterization of transient low-population states of biological macromolecules and their complexes. *Chem Rev* 109(9):4108–4139.
40. Shao X, Fernandez I, Südhof TC, Rizo J (1998) Solution structures of the Ca2+-free and Ca2+-bound C2A domain of synaptotagmin I: Does Ca2+ induce a conformational change? *Biochemistry* 37(46):16106–16115.
41. Choi UB, et al. (2010) Single-molecule FRET-derived model of the synaptotagmin 1-SNARE fusion complex. *Nat Struct Mol Biol* 17(3):318–324.
42. Vrljic M, et al. (2010) Molecular mechanism of the synaptotagmin-SNARE interaction in Ca2+-triggered vesicle fusion. *Nat Struct Mol Biol* 17(3):325–331.
43. Chicka MC, Hui E, Liu H, Chapman ER (2008) Synaptotagmin arrests the SNARE complex before triggering fast, efficient membrane fusion in response to Ca2+. *Nat Struct Mol Biol* 15(8):827–835.
44. Honigmann A, et al. (2013) Phosphatidylinositol 4,5-bisphosphate clusters act as molecular beacons for vesicle recruitment. *Nat Struct Mol Biol* 20(6): 679–686.
45. Wang P, Wang CT, Bai J, Jackson MB, Chapman ER (2003) Mutations in the effector binding loops in the C2A and C2B domains of synaptotagmin I disrupt exocytosis in a nonadditive manner. *J Biol Chem* 278(47):47030–47037.
46. Takamori S, et al. (2006) Molecular anatomy of a trafficking organelle. *Cell* 127(4): 831–846.
47. Banerjee S, Huber T, Sakmar TP (2008) Rapid incorporation of functional rhodopsin into nanoscale apolipoprotein bound bilayer (NABB) particles. *J Mol Biol* 377(4): 1067–1081.
48. Brewer KD, Li W, Horne BE, Rizo J (2011) Reluctance to membrane binding enables accessibility of the synaptobrevin SNARE motif for SNARE complex formation. *Proc Natl Acad Sci USA* 108(31):12723–12728.
49. Delaglio F, et al. (1995) NMRPipe: A multidimensional spectral processing system based on UNIX pipes. *J Biomol NMR* 6(3):277–293.
50. Johnson BA, Blevins RA (1994) NMR View: A computer program for the visualization and analysis of NMR data. *J Biomol NMR* 4(5):603–614.